Atomic and optical properties of warm dense copper

Gennady Miloshevsky[*] and Ahmed Hassanein

Center for Materials under Extreme Environment, School of Nuclear Engineering, Purdue University,
400 Central Drive, West Lafayette, Indiana 47907-2017, USA

The emission of x rays from warm dense matter is of great interest for both spectroscopic diagnostics and development of intense x-ray sources. We report the results from the collisional-radiative steady-state (CRSS) modeling of atomic and optical properties of copper plasmas at near-solid and solid-state density for a range of temperatures. The CRSS model is validated against the available data on the average charge state and shifts of energy levels in aluminum and the opacity and emissivity spectra of carbon and aluminum plasmas. The average charge states, number density of ion species, and free electrons as a function of temperature are investigated for the solid-density copper plasma. Due to the dense plasma environment the four outer electrons are found to be unbounded even in the low-temperature limit ~ 1 eV. As the temperature changes from 1 to 100 eV, the predominant species vary from fivefold- to twelvefold-ionized copper ions. The opacity and emissivity spectra of dense copper plasmas are studied using the local thermodynamic equilibrium (LTE) and non-LTE approaches. It is found that the non-LTE effects are important in the spectral region of soft x rays emitted from the K shell. The emissivity in spectral lines is completely suppressed, indicating the importance of the energy-dissipating radiative processes in this soft x-ray region. Line broadening and redshifts of the K- and L-shell spectral lines toward higher wavelengths are observed with the increase of plasma density. These results have important implications for understanding the radiative properties of warm dense copper and can be useful for future experimental studies.

I. INTRODUCTION

Radiative properties of dense plasmas are of great importance in many research fields such as inertial confinement fusion [1,2], x-ray free-electron lasers [3,4], and astrophysical plasmas [5]. On one side, dense plasmas can serve as an intense source of x-ray and ultraviolet (UV) radiation. On the other side, x-ray lasers can be used to probe the ion structure, electronic charge states, and thermodynamic and optical properties of dense plasmas [6]. Equations of state, compositions, and transport and optical properties of dense plasmas [7,8] are also needed for radiation hydrodynamic simulations as well as for interpretation of plasma emission spectra. Radiation emitted from dense plasmas carries information about plasma conditions and therefore it is also an important diagnostic tool [9]. Due to the development of intense x-ray free-electron lasers it has become possible to gain a fundamental understanding of the transition between cold solid and hot plasma conditions. This transient state is referred to as warm dense matter (WDM) [10]. The WDM regime is characterized by comparable thermal and Fermi energies and strong ion-ion coupling. The radiative properties of WDM are not well known [11]. Describing and characterizing the optical properties of the WDM state associated with temperatures of 1–100 eV and 0.01–10 times the solid density are extremely difficult both theoretically and experimentally. Theoretically it is difficult because the electron degeneracy, strong correlation of ions, and quantum effects should be treated. The computational approaches are often based on various assumptions about the charge state of ions and electronic structure of dense plasmas. Measurements are challenging because WDM is a fast transient state on a

nanosecond time scale under laboratory conditions [12]. It is difficult to create a uniform, well-defined WDM state and then precisely characterize it. The experimental uncertainty in the emissivity of WDM is relatively large [13]. Therefore the computational prediction of the emission spectra of WDM is important compared to performing experiments.

In order to calculate opacities and emissivities, the details about the electronic structure of a plasma are required [14]. These details include the bound-state electron populations of ions and the average degree of ionization (average number of free electrons per ion) [15]. The self-consistent, accurate modeling of the atomic properties and the electronic and ionic structure is needed to calculate these two quantities in the WDM regime. The charge state of ions can be changed through various collisional and radiative processes such as excitation, deexcitation, ionization, and recombination. The primary sources of radiation emission from plasma are bound-bound, free-bound, and free-free transitions of electrons. The observed spectra are strongly influenced by the atomic structure of the ions and the distribution among bound negative-energy electrons and free positive-energy electrons [15]. In dense plasma, the energy levels of the bound states and electron degeneracy are modified by neighboring plasma electrons and ions. The ionization potentials of bound states and electron occupancies of energy levels are changed due to pressure ionization [16]. Radiative opacities and emissivities are also affected by the ionization balance. It is therefore important to understand the factors that influence the electron and ion charge distributions in plasmas at near-solid density.

The approximation of local thermodynamic equilibrium (LTE) is usually assumed to be valid at high plasma densities in the WDM regime where collisions prevail [17–19]. Although some fraction of energetic photons can be absorbed in dense plasma, this may not have a significant influence on the ionization-excitation balance. The Saha-Boltzmann equations

*gennady@purdue.edu

[20] can then be used in this case to calculate the electron occupancies of energy levels in the ions and the number density of free electrons. However, the level populations in inhomogeneous plasmas with spatial- and time-varying temperature and density gradients cannot be represented using the Saha-Boltzmann description. The density effects on the atomic structure of energy levels and the presence of bound and high-energy free electron fractions in dense plasma may also result in a nonequilibrium thermodynamic state (non-LTE) [21]. The evidence for out-of-equilibrium states in warm dense matter probed by x-ray Thomson scattering was recently demonstrated [22]. Depending on the geometry, size, and thermodynamic properties of the plasma, the clear boundary between the LTE and non-LTE states is not well established [17]. The collisional-radiative kinetics models were used to calculate the level populations in non-LTE plasmas [21,23–26]. When the collisional and radiative processes are important, the collisional-radiative approach based on rigorous atomic physics provides a more realistic model to characterize and analyze the photon emission spectra, the equations of state, the ion composition, and the number of free electrons. The rate equations are solved that describe the change of the electron population of each energy level due to all possible collisional and radiative transitions and reactions from other energy levels. The full set of rate equations including all transitions for each level is very large. The complexity of rate equations is reduced by treating the rates of radiative absorption and emission due to nonlocal radiation fields from the surrounding plasma in the escape factor approximation [27]. The decrease in the ionization potential with increasing plasma density results in the release of the uppermost energy levels to the continuum and they are ignored in the rate equations. These simplifications reduce the computational cost of collisional-radiative kinetics calculations.

In this paper we report the opacity and emissivity of copper plasma at temperatures from 20 to 100 eV and densities ranging from $0.01\rho_0$ to ρ_0, where $\rho_0 = 8.92$ g/cm^3 is the solid-state density of copper. This range of plasma conditions covers the upper-left portion of the temperature-density phase space of the WDM regime. The self-consistent modeling is based on collisional-radiative kinetics calculations including such effects as pressure ionization, continuum lowering, delocalized electrons, spectral line broadening, and spectral and energy level shifts. These models are implemented in the REODP computer code. REODP is an acronym that stands for radiative emissivity and opacity of dense plasmas. The computational models are described in Sec. II. In Sec. III, the average charge state, energy level shifts, opacities, and emissivities are validated against the results available in the literature. The influence of temperature and density in this phase region of WDM on the bound-state electron populations and emissivities of copper plasma in soft x-ray and UV spectral regions is also analyzed in Sec. III. The LTE and non-LTE emissivities are compared. The conclusions are drawn in Sec. IV.

II. COMPUTATIONAL MODELS

The theoretical and computational framework of our study is described in this section. This includes the calculation of atomic data and plasma properties. Knowledge of the atomic data allows determination of the density of free electrons, the electron population of bound levels of ions, and the absorption and emission coefficients in a range of plasma temperatures and densities.

A. Atomic and non-LTE plasma models

To derive the atomic data required for the collisional-radiative kinetics calculations, the self-consistent solution of the Hartree-Fock-Slater (HFS) equations is used. For many-electron atoms or highly charged ions where the solution of the more accurate Hartree-Fock equations is very difficult due to the presence of the nonlocal exchange terms, the HFS approximation gives surprisingly good results for wave functions and energy levels. The atomic model has been described in previous work [28–30]. We briefly summarize here the main points. The nuclear and electronic degrees of freedom in the many-body Schrödinger equation are separated using the Born-Oppenheimer approximation. The total wave function is then approximated by a single Slater determinant made up of one-electron spin orbitals. Each electron is assumed to move in the mean field of all the other electrons. The wave function is separated into radial, angular, and spin parts by applying the central-field approximation. In this way, the electronic Schrödinger equation is reduced to a system of single-electron HFS equations with an effective potential. The effective potential is the sum of the nuclear and electronic Coulomb potentials and the exchange potential. The exchange potential for different orbitals in the HFS method is replaced by Slater's orbital-independent exchange potential formed by averaging over the orbital exchange potentials [31]. The exchange term describes the Fermi correlation between electrons with the same spin, preventing them from being located at the same point in space. Since the potentials are expressed through the wave functions, the radial HFS equations are solved for each orbital using iterative techniques. The relativistic effects and spin-orbit interactions are taken into account in the scope of perturbation theory [32]. The dynamic and static electron correlations missing in the HFS theory are included using multiconfiguration and configuration-interaction methods [33,34]. A list of electron configurations and their mixing coefficients used in the multiconfiguration HFS calculations is provided in Table I for carbon, aluminum, and copper atoms. The artifacts of the HFS approach such as the electrons' motions with respect to each other (dynamic correlation) and the proper arrangement of electrons around the nucleus (static correlation) are fixed. The wave functions, atomic energy levels, ionization potentials, oscillator strengths, transition probabilities, photoionization cross sections, broadening constants, and other atomic data for all types of ions existing in plasma are calculated as a result of the solution of the HFS system.

The atomic data derived from the HFS model are used in the collisional-radiative steady-state (CRSS) model [29,30]. This non-LTE CRSS model is applied for calculating the ionization balance, collisional excitation and ionization rates, radiative transition probabilities, radiative and dielectronic recombination rates, and absorption and emission coefficients. The collisional processes involve collisional excitation and deexcitation, collisional ionization, and three-body

TABLE I. The list of electron configurations and mixing coefficients c_i for carbon, aluminum, and copper atoms used in the multiconfiguration HFS calculations.

C $2s^2 2p^2$ ^3P		Al $2p^6 3s^2 3p$ ^2P		Cu $3p^6 3d^{10} 4s$ ^2S	
Configuration	c_i	Configuration	c_i	Configuration	c_i
$2s^2 2p^2$	0.9686	$2p^6 3s^2 3p$	0.97760	$3p^6 3d^{10} 4s$	0.99754
$2p^4$	0.1339	$2p^6 3p^3$	0.19849	$3p^5 3d^{10} 4s 4p(^3P)$	−0.04043
$2s 2p^2 3d(^2D)$	0.1070	$2p^4(^1S)3s^2 3p 3d^2(^2P)$	0.03327	$3p^6 3d^8 4s 4p^2(^2D)$	−0.02516
$2s 2p^2(^2P)3s$	0.0711	$2p^4(^3P)3s^2 3p 3d^2(^4D)$	−0.02753	$3p^6 3d^8 4s 4p^2(^2S)$	0.02485
$2s 2p^2 3d(^2P)$	−0.0662	$2p^4(^1D)3s^2 3p 3d^2(^2F)$	−0.02427	$3p^5 3d^{10} 4s 4p(^1P)$	−0.02152
$2s 2p^2 3d(^4P)$	0.0655	$2p^4(^3P)3s^2 3p 3d^2(^4P)$	−0.02133	$3p^4 3d^{10} 4s 4p^2(^2D)$	0.01926
$2s 2p(^3P)3s 3p(^2P)$	0.0600	$2p^4(^1D)3s^2 3p 3d^2(^2D)$	−0.02050	$3p^6 3d^8 4s 4p^2(^4P)$	−0.01874
$2s^2 3p^2$	−0.0451	$2p^4(^3P)3s^2 3p 3d^2(^2D)$	−0.01946	$3p^4 3d^{10} 4s 4p^2(^4P)$	0.01382
$2s^2 3d^2$	0.0350	$2p^4(^1D)3s^2 3p 3d^2(^2P)$	−0.01589	$3p^6 3d^8 4s 4p^2(^2P)$	−0.01352
$2p^2 3d^2$	−0.0315	$2p^4(^3P)3s^2 3p 3d^2(^2P)$	−0.01506	$3p^6 3d^9 4p^2$	−0.01221
$2p^3(^2D)3p$	−0.0295	$2p^4(^3P)3s^2 3p 3d^2(^4S)$	−0.01231	$3p^4 3d^{10} 4s 4p^2(^2S)$	−0.01201
$2p^2 3s^2$	−0.0271	$2p^4(^3P)3s^2 3p 3d^2(^2S)$	−0.00870	$3p^4 3d^{10} 4s 4p^2(^2P)$	0.00994
$2s 2p^2(^4P)3s$	0.0266	$2p^4(^1S)3p^3 3d^2(^2P)$	0.00678	$3p^5 3d^9 4s^2 4p(^1P)$	0.00676
$2p^3(^2P)3p$	−0.0263	$2p^5 3s 3p(^3P)3d(^3P{}^3D)$	0.00602	$3p^3(^2D)3d^{10} 4s 4p^3(^3D)$	−0.00206
$2s 2p(^1P)3s 3p(^2P)$	0.0256	$2p^5 3s 3p(^1D)3d(^3P{}^3F)$	−0.00588	$3p^5 3d^9 4s^2 4p(^3P)$	−0.00203
$2s 2p(^3P)3s 3p(^4P)$	−0.0253	$2p^4(^3P)3p^3 3d^2(^4D)$	−0.00562	$3p^3(^2P)3d^{10} 4s 4p^3(^3P)$	0.00181
$2s 2p^2 4s$	0.0244	$2p^5 3s 3p(^3P)3d(^1P{}^3D)$	−0.00560	$3p^5 3d^8(^1S)4s 4p^3(^3P)$	−0.00148
$2p^3(^4S)3p$	0.0232	$2p^4(^1D)3p^3 3d^2(^2F)$	−0.00495	$3p^5 3d^8(^1D)4s 4p^3(^3D)$	0.00140
$2p^2 3p^2$	0.0200	$2p^5 3s 3p^2(^1S)3d(^3P)$	−0.00447	$3p^3(^2D)3d^{10} 4s 4p^3(^1D)$	−0.00117
$2s 2p^2 4d$	0.0155	$2p^5 3s 3p^2(^1D)3d(^1P{}^1F)$	−0.00443	$3p^3(^2P)3d^{10} 4s 4p^3(^1P)$	0.00103
$2s 2p(^3P)3d 4f(^4F)$	0.0150	$2p^4(^3P)3p^3 3d^2(^4P)$	−0.00435	$3p^5 3d^8(^3P)4s 4p^3(^3D)$	−0.00089
$2s 2p 3p 3d$	0.0147	$2p^5 3s 3p^2(^3P)3d(^3P{}^1D)$	0.00426	$3p^3(^4S)3d^{10} 4s 4p^3(^5S)$	−0.00088
$2s 2p(^3P)3d 4f(^2F)$	−0.0144	$2p^4(^1D)3p^3 3d^2(^2D)$	−0.00417	$3p^5 3d^8(^1S)4s 4p^3(^1P)$	−0.00080
$2s 2p(^3P)3d 4f(^2D)$	0.0134	$2p^4(^3P)3p^3 3d^2(^2D)$	−0.00397	$3p^5 3d^8(^3P)4s 4p^3(^3P_0)$	−0.00075
$2s 2p 3d 4p$	0.0121	$2p^4 3s^2 3p^3$	0.00375	$3p^5 3d^8(^1D)4s 4p^3(^1D_0)$	0.00073
$2s 2p(^1P)3d 4f(^2F)$	−0.0120	$2p^5 3s 3p^2(^1D)$	−0.00363	$3p^5 3d^8(^1D)4s 4p^3(^3P)$	−0.00069
$2s 2p 3p 4d(^2D)$	0.0113	$2p^5 3s 3p^2(^3P)3d(^3P_0)$	0.00348	$3p^3(^4S)3d^{10} 4s 4p^3(^3S)$	−0.00067
$2p^3 4p$	0.0109	$2p^5 3s 3p^2(^3P)$	−0.00325	$3p^5 3d^8(^3P)4s 4p^3(^5S)$	0.00065
$2s 2p 3p 4d(^4D)$	−0.0106	$2p^4(^1D)3p^3 3d^2(^2P)$	−0.00324	$3p^5 3d^8(^3P)4s 4p^3(^1D)$	−0.00056
$2s 2p 4s 4p$	0.0101	$2p^5 3s 3p^2(^3P)3d(^1P{}^3P)$	−0.00322	$3p^6 3d^6 4s 4p^4$	0.00055

recombination. The radiative processes are spontaneous and stimulated transitions, photorecombination, and dielectronic recombination. Nonlocal radiation transport effects such as photoexcitation and photoionization that influence the ion populations are included in the rate equations using the escape factor approximation [27]. The spontaneous emission rates for radiative transitions are reduced by an escape factor, which accounts for depopulation of upper quantum states by reabsorption of nonlocal photons. The system of rate equations is solved numerically and the populations of atomic levels are calculated for all the ions in the plasma. Once the populations and number densities of ion species and free electrons are determined, the spectral opacity and emissivity of the plasma can be calculated. A time-dependent treatment of the ion populations is also possible with our CRSS model as described in Ref. [30]. A detailed description of the calculation of atomic data and CRSS model is given in Refs. [29,30].

B. Dense plasma effects

For high-density plasmas, the effect of the plasma environment on the electron population of atomic levels of ions and the number density of free electrons should be considered

[11]. The outer electrons can be severely perturbed by the presence of the dense plasma environment. The nearby ions play a significant role, leading to effects such as alterations of the electronic structure and energy levels of ions, reduction of ionization potentials, spectral line shift and broadening, and changes in line shapes and absorption and emission spectra. At high densities, the wave functions of several neighboring ions can overlap forming quasi-molecules [15]. It is difficult to take such effects into account in a consistent way in the framework of the quantum HFS description due to the large number of involved ions. In low-temperature and high-density plasma, the ions are packed tightly. A sphere that encloses the nucleus, bound electrons, and free electrons of each ion can be considered as an appropriate model [35]. Charge neutrality is satisfied inside the ion sphere volume with a uniform electron distribution. Beyond the ion sphere the plasma is assumed to be an electrically neutral background.

The atomic data calculated for the isolated ions are used in the CRSS model with the ionization potential depression (continuum lowering) taken into account by the Stewart and Pyatt model [36,37]. It was recently demonstrated using a two-step HFS approach that this model can accurately describe the experimental data on dense aluminum plasmas [38]. The

ionization potential I_i of the ith ion is reduced by the value $\Delta I_i = I_i - I_i'$ which is calculated as

$$\Delta I_i = \frac{3}{2} \frac{\text{Ry}\, a_0\, i}{R_i} \left\{ \left[1 + \left(\frac{R_D}{R_i} \right)^3 \right]^{2/3} - \left(\frac{R_D}{R_i} \right)^2 \right\}, \quad (1)$$

where I_i' is the lowered ionization potential of the ith ion in a dense plasma, i is the ion charge or the number of electrons removed from the ion, Ry is the Rydberg constant, a_0 is the Bohr radius, $R_i = [(3\,i)/(4\pi\, n_e)]^{1/3}$ is the ion-sphere radius of the ith ion, n_e is the density of free electrons, $R_D = \sqrt{kT_e/[4\pi\, n_e(1 + \bar{Z})\, e^2]}$ is the Debye radius, T_e is the electron temperature, and $\bar{Z} = n_e/n$ and n are the average charge state and the number density of the ions. Equation (1) interpolates between the low-density Debye screening and the high-density ion-sphere limit. The reduction ΔI_i results in lowering of the continuum level, shifts of bound-electron energy levels towards the continuum, and disappearance of bound states. All the energy levels are shifted by the same amount (to first approximation), so that the energy difference between the levels is not changed [15]. As the plasma density increases, the orbitals with energies above the lowered ionization potential I_i' are treated as ionized. The energy levels belonging to those orbitals are removed from the CRSS rate equations. This procedure reduces the number of bound electron states in the ions.

The shift in positions of spectral lines, called the polarization shift, is occurred in dense plasmas. The polarization induced by free electrons modifies the energy of photons emitted during a transition between two levels [15]. Assuming uniform electron distribution in the ion sphere, the shift of a spectral line in the ith ion is calculated as follows:

$$\Delta \varepsilon_i = \frac{1}{2} \frac{i\, e^2}{R_i^3} \left(r_b^2 - r_a^2 \right), \quad (2)$$

where $r_a^2 = \langle a | r^2 | a \rangle$ and $r_b^2 = \langle b | r^2 | b \rangle$ are the average values of the square of the radial distance r in the initial state $|a\rangle$ and the final state $|b\rangle$ of photon transition between two discrete energy levels. The values of r_a^2 and r_b^2 are determined from the HFS model. The line shift $\Delta \varepsilon_i$ is negative, meaning that the photon wavelength is increased (redshift). The wavelength shift of spectral lines is rather small. Its experimental measurement is a difficult problem, since it competes with the line broadening.

The reduction in continuum or "continuum lowering" due to pressure ionization also affects the collisional and radiative rates through the change of the ionization state of the ions. Therefore, the rate coefficients of the atomic processes implemented in the CRSS model [30] are modified. The modification of coefficients mainly involves the incorporation of the potential reduction ΔI_i into the rate equations. At near or above solid density, the removal of bound electron states above the continuum level is implemented. By including ΔI_i into the Lotz formula [30], the collisional ionization rate is corrected in order to account for the effect of ionization potential lowering. The correction factor to the ionization rate is determined, and in accordance with the detailed balance it is applied to correct the three-body recombination rate. However, the pressure ionization also affects the relation

between the ionization and recombination rates. Therefore, the three-body recombination rate is additionally multiplied by an exponential factor accounting for ΔI_i. The corrections to radiative and dielectronic recombination rates are neglected since at high densities the main recombination process is the three-body recombination. The HFS and CRSS models accounting for dense plasma effects are implemented in the REODP code.

III. RESULTS AND DISCUSSION

In this section we present a comparison of our results on the average charge state and ground-state energy levels of warm dense aluminum with predictions from simulations using different computational approaches [16]. Opacities and emissivities of dense carbon and aluminum plasmas are also validated against the available data [18,26,39,40]. The average charge state, spectral LTE and CRSS (non-LTE) opacities and emissivities of warm dense copper plasma are investigated and discussed.

A. Benchmarking the REODP code

The atomic model described in Sec. II is used to evaluate the effect of a dense plasma environment on the average charge state of aluminum ions. The free electrons distributed around the ions in dense plasma reduce the binding energy of the bound electrons. At high densities the binding energy of electrons may vanish and the bound states shift into the continuum. This is because the attraction of the bound electrons toward the nucleus is decreased due to the shielding of the nuclear potential by the free electrons [15]. To illustrate the influence of dense plasma on the atomic properties of the ions, we show in Fig. 1(a) the average charge state of aluminum ions at solid-state density $\rho_0 = 2.7\,\text{g/cm}^3$ as a function of plasma temperature. Our REODP results are validated against the available data reported in Ref. [16]. It can be seen in Fig. 1(a) that, at temperature $\sim 5\,\text{eV}$, the $n = 3$ states of aluminum ions (three electrons in the $3s$ and $3p$ orbitals) are no longer bound. The average charge state $\bar{Z} = 3$ is correctly predicted by our model, UBCAM [16], and density functional theory (DFT) [41] models in the range of plasma temperatures from ~ 5 to $\sim 15\,\text{eV}$. Predictions of $\bar{Z}$ by the SESAME [42] and quotidian equation of state (QEOS) [43] models deviate from $\bar{Z} = 3$, since these models are based on the classical Thomas-Fermi approach [44]. At higher temperatures $> 20\,\text{eV}$, the agreement is rather good from all models. It can be seen in Fig. 1(a) that the average charge $\bar{Z}$ of dense aluminum plasma increases linearly with temperature, reaching $\bar{Z} \approx 7$ at $\sim 80\,\text{eV}$. For these plasma conditions, the emission spectra can be strongly affected by the most abundant sevenfold-ionized ions. In Fig. 1(b) the average charge state of aluminum plasma is plotted as a function of compression ratio ρ/ρ_0 at temperature $12.5\,\text{eV}$, where $\rho_0 = 2.7\,\text{g/cm}^3$ is the solid density of aluminum. This figure also gives a comparison between the predictions of the charge state of aluminum from our and other models [16]. There is disagreement between models at compression ratios less than ~ 0.4. The charge state $\bar{Z}$ predicted from our REODP code is close to that calculated from the UBCAM model. In the density range from ~ 1 to $\sim 20\,\text{g/cm}^3$
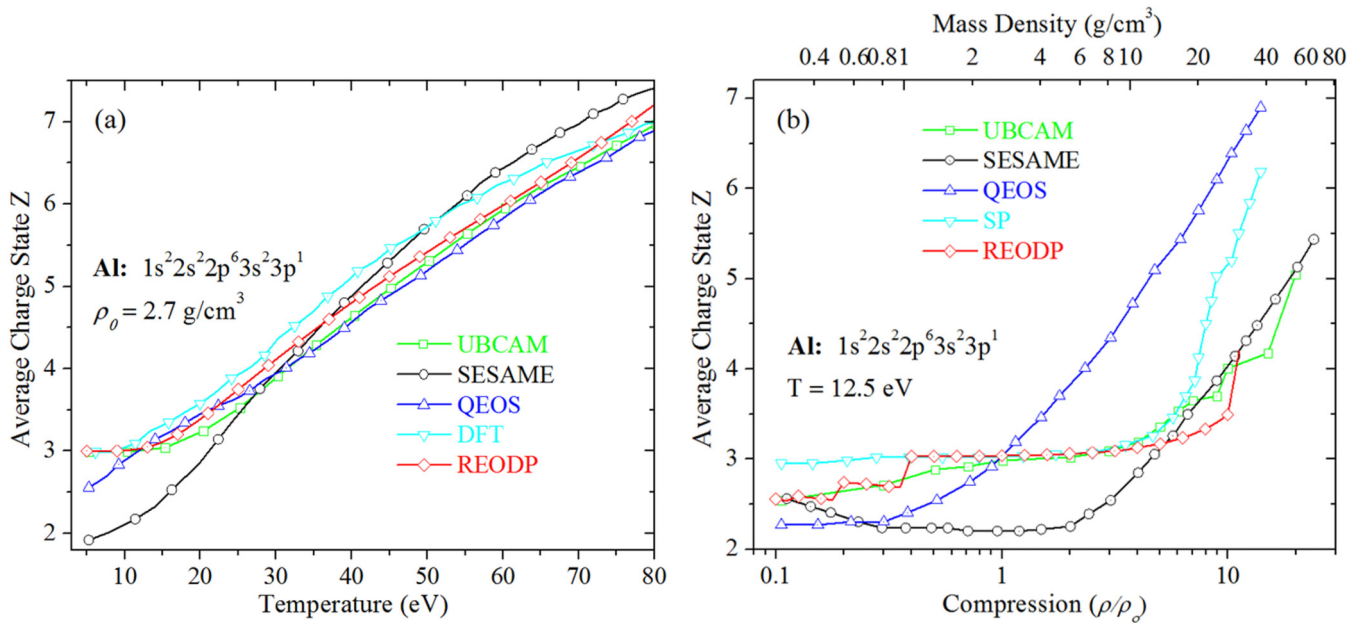
FIG. 1. (Color online) The average charge state $\bar{Z}$ of aluminum at solid-state density $\rho_0 = 2.7 \, \text{g/cm}^3$ as a function of temperature (a) and compression ratio ρ/ρ_0 at a temperature of 12.5 eV (b). The present results (red line with open rhombs) are compared with the data derived from different models and reported in Ref. [16].

[top scale in Fig. 1(b)], the charge state is $\bar{Z} \sim 3$, predicted by REODP, UBCAM, and Stewart and Pyatt (SP) [36] models. The SESAME and QEOS models demonstrate quite different behavior of $\bar{Z}$. A rapid increase in $\bar{Z}$ occurs near the tenfold compression [Fig. 1(b)]. The pressure ionization of the $2p$ shell electrons of aluminum is responsible for this effect. The observed distinctions in $\bar{Z}$ from different models resulting in different ionic species in aluminum plasma can significantly affect the opacity and emission spectra.

The reduction of the binding energy of two ionic states of Al IV and Al V ions as a function of compression ratio is shown in Fig. 2 for a plasma temperature of 12.5 eV. This phenomenon of binding energy reduction of electrons with the increase of plasma density is known as continuum lowering [15]. Our REODP results are compared with computations carried out with the UBCAM and SP approaches [16]. The agreement is fairly good, especially with the SP model. It can be seen in Fig. 2 that the $2p$ energy levels are shifted into
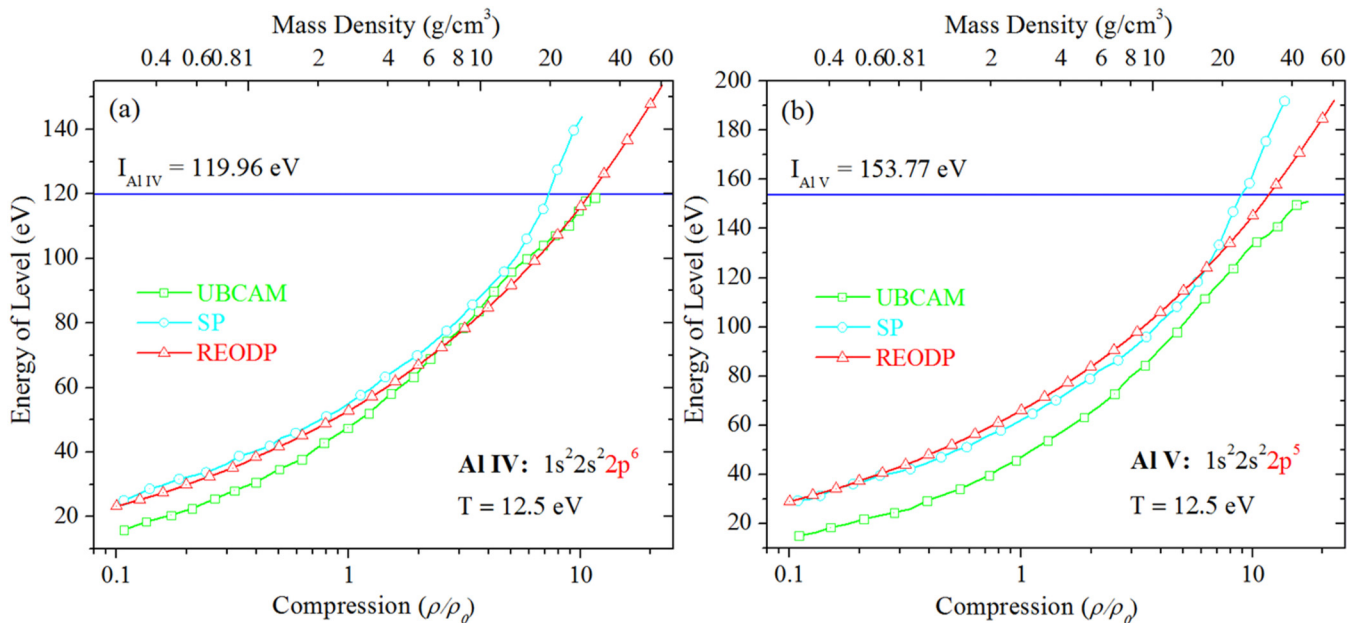

FIG. 2. (Color online) The ground-state energy levels of Al IV (a) and Al V (b) ions as a function of compression ratio ρ/ρ_0 at a temperature of 12.5 eV. The results from different models reported in Ref. [16] are compared with the present data (red line with open triangles). Horizontal blue lines are the ionization potentials of Al IV and Al V ions.
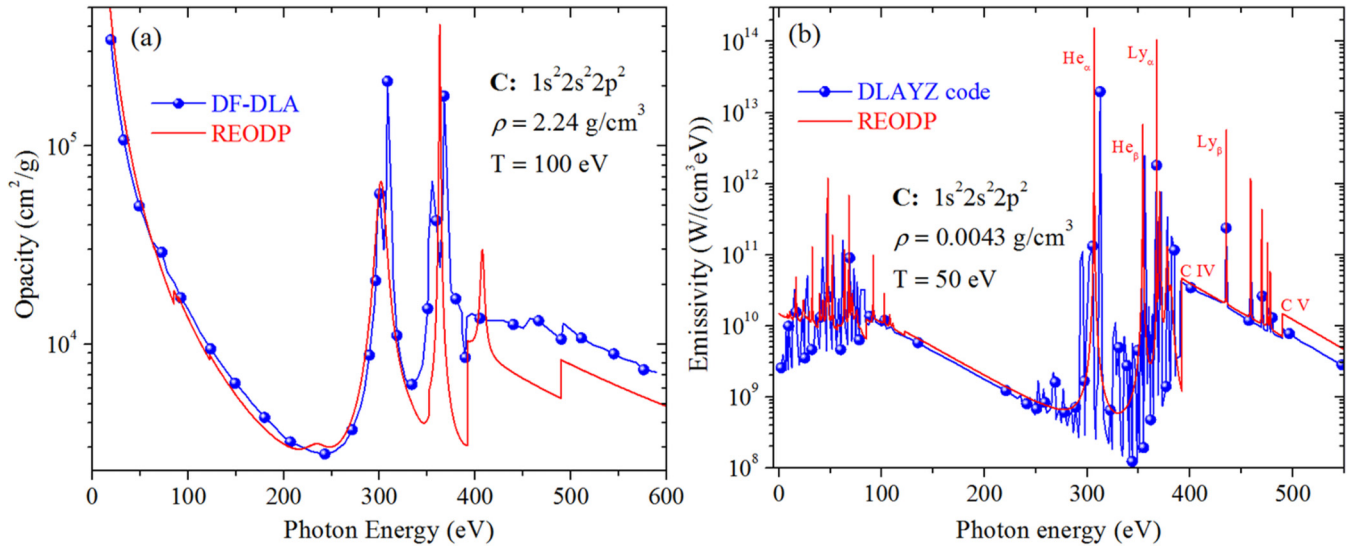
FIG. 3. (Color online) Comparison of opacity (a) and emissivity (b) of carbon plasma as a function of photon energy. The present results are denoted by solid red lines, whereas DF-DLA data [18] (a) and the result calculated from the DLAYZ code [26] (b) are represented as solid blue lines with filled circles.

the continuum and become pressure ionized at a compression ratio of $\rho/\rho_0 \sim 10$. This explains why $\bar{Z} \sim 3$ in a wide range of plasma density [Fig. 1(b)]. The ionization of $2p$ electrons (horizontal lines in Fig. 2) is reached only at about tenfold compression. It is interesting to note that the $2p^5$ and $2p^6$ energy levels are approximately shifted in parallel to each other by a constant value [the curves in Figs. 2(a) and 2(b) are very similar]. Therefore, to first approximation, the energy difference between the $2p^5$ and $2p^6$ levels and the energy of emitted photons are not changed.

The radiative opacity (mass absorption coefficient) of carbon plasma at a density of 2.24 g/cm^3 and temperature of 100 eV calculated from our REODP code is compared in Fig. 3(a) with the spectral opacity derived from the detailed level accounting (DLA) model based on the Dirac-Fock (DF) approach for calculating the atomic data [18]. Although the DF-DLA model is more accurate, it can be seen in Fig. 3(a) that absorption spectra and spectral line positions from the two models are in rather good agreement. The photon absorption peaks are located in the energy range of 0–100 eV and 280–420 eV. The free-free absorption contributes to the region of the continuous spectrum below $\sim$100 eV. The absorption lines within the spectral region spanning from $\sim$280 to $\sim$420 eV (the K edge) are due to the $1s-2p$ transitions of He-like and H-like carbon ions (C V and C VI). The spectral peaks and absorption thresholds at higher photon energy >420 eV originate from the $1s-np$ ($n \geqslant 3$) transitions of H-like carbon ions. The emission spectrum of carbon plasma at a temperature of 50 eV and plasma density of 0.0043 g/cm^3 was calculated using the DLAYZ code and reported in Ref. [26]. Comparison of this emission spectrum with that calculated from our REODP code is illustrated in Fig. 3(b). The DLAYZ spectrum shows more details of the spectral lines since it is based on the DF-DLA model which is more accurate. However, it is seen in Fig. 3(b) that the agreement between the two emission spectra is very good in the continuum regions as well as in the location of spectral lines. The spectral lines located in the

energy range below $\sim$100 eV are generated by the transitions of the outermost electrons, while those localized between 250 and 500 eV are due to the transitions of inner-shell electrons. The $1s$ ionization thresholds of C IV and C V ions and the He-α, He-β, Lyman-α, and Lyman-β emission lines are labeled in Fig. 3(b). The agreement in spectra indicates that the charge-state distribution of carbon ions and the excited-state populations of the electrons are computed properly in our REODP code. It should be noted that absolute units of opacity and emissivity are used in Fig. 3 for spectral comparisons.

The radiative opacity of aluminum plasma at a density of 1 g/cm^3 and temperature of 400 eV is plotted in Fig. 4(a) and compared with the spectrally resolved opacity calculated using the multiconfiguration Dirac-Fock (MCDF) model in the LTE approximation [39]. A very good agreement between the two opacities expressed in physical units of cm^2/g can be seen. The spectral lines in the energy range of 1500–1800 eV are generated by the electrons from the $1s-2p$ transitions (K shell). The other K-shell peaks nearby, $\sim$1860, $\sim$1950, and $\sim$2030 eV are due to higher-order $1s-3p$ and $1s-4p$ transitions. The M-shell and L-shell transitions contribute to the spectral lines located near $\sim$140 and $\sim$270 eV. As a final example, we show in Fig. 4(b) a comparison of our calculated absorption coefficient of aluminum plasma at a density of 0.025 g/cm^3 and temperature of 0.826 eV (10 000 K) with that derived from quantum molecular dynamics (QMD) simulations [40]. It should be noted that the QMD simulation of optical properties is based on a model of dielectric response functions involving the Kubo-Greenwood formulation that is absolutely different from collisional-radiative plasma models. Nevertheless, the agreement between absorption spectra obtained from different computational approaches is very good. The location and magnitude of the spectral line of the neutral aluminum atom at $\sim$5.2 eV corresponding to the $3s-3p$ transition is well reproduced. To summarize, the comparison of the average charge states, depression of energy levels, and opacity and emissivity spectra with the available data published in the
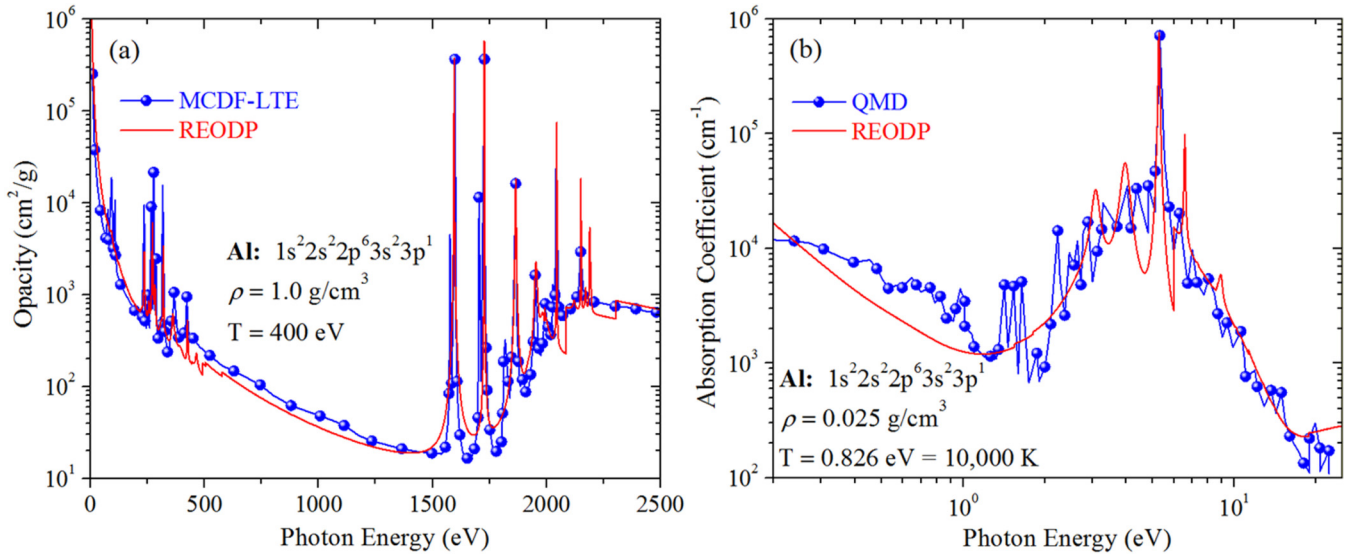
FIG. 4. (Color online) Comparison of opacity (a) and absorption coefficient (b) of aluminum plasma as a function of photon energy. The present results are shown as solid red lines, whereas MCDF-LTE [39] (a) and QMD [40] (b) data are represented as solid blue lines with filled circles.

literature demonstrates that our REODP code can be used to study the optical properties in the WDM regime.

B. Atomic and optical properties of dense copper plasma

The average charge of the ions in plasma depends on the electron temperature and ion density. The number density of free electrons and the average charge state of copper ions are plotted in Fig. 5(a) for the solid density as a function of the temperature. The scales of these variables are shown on the left-hand side and the right-hand side of this figure since these curves coincide. It is seen in Fig. 5(a) that even at low temperatures, ~1 eV, the four outer electrons from the $3d$ and $4s$ shells are ionized (scale in red on the right-hand side) in solid-state warm copper. At such high density the dominant charge state $\bar{Z}$ becomes the highly ionized ionic species as the plasma temperature increases from ~10 to ~100 eV. At temperature ~100 eV the number density of free electrons is ~10^{24} cm^{-3} and the most abundant species are the 12-fold-ionized copper ions. The charge-state distribution for the copper plasma of the solid-state density as a function of temperature is illustrated in Fig. 5(b). It is seen that the lowest charge state corresponds to the Cu V ions. The ionic charge states with an electron in the $4s$ orbital and three electrons in the $3d$ orbital do not survive the ionization potential lowering due to density effects. The warm dense copper plasma is thus composed from Cu V at ~1 eV to Cu XII at ~100 eV. At this high temperature ~100 eV, the $3d$ shell of copper is completely ionized. The general feature of the charge-state distribution of copper ions is that the partial density of the most abundant charge state shifts toward the highly charged ions as the temperature increases.

One of the interesting results of these studies is the observation that the K-shell and L-shell line opacity of dense copper plasmas deviates from the LTE state. The LTE model was implemented and used for solving the Saha-Boltzmann equations [15] in order to determine the atomic

level populations, the charge state of ions, and the fraction of free electrons under the LTE conditions. In Fig. 6 the spectrally resolved K-shell and L-shell opacities of copper plasma at 100 eV as a function of photon wavelength are shown for various densities. The wavelength range of photons under consideration here corresponds to soft x rays. It is seen that the LTE model overestimates the K-shell and L-shell opacities as compared to the result of the non-LTE (HFS-CRSS) approach. This indicates that the radiative processes due to soft x rays that populate and depopulate the ionic states are not negligible. The LTE model does not describe properly the degree of ionization and the ionic population distributions. The discrepancy between the LTE and non-LTE opacity is considerably higher for the K-shell spectrum [Fig. 6(a)] as compared to that of the L-shell spectrum [Fig. 6(b)]. For the K-shell opacity, the LTE result shows strong spectral lines, which are completely suppressed in the non-LTE spectrum [Fig. 6(a)]. The disagreement between the LTE and non-LTE opacities of the L-shell lines is significantly smaller [Fig. 6(b)]. The effect of plasma density on the K-shell and L-shell line opacity in the soft x-ray region is also clearly seen in Fig. 6. There are two interesting features in these x-ray spectra, the shift of spectral lines toward higher wavelength (redshift) as the plasma density increases and the line broadening at higher densities. It is seen in Fig. 6 that the shift of photon wavelength is relatively small. This shift of spectral lines is due to the modification of the electrostatic potential by the free electron distribution near the bound electron orbits. The wavelength shift of spectral lines was reported in previous work [18,39,45]. It should be noted that the line shifting interferes with the broadening of lines. As the density increases, the spectral lines are both shifted and broadened. The opacity of absorption lines is also reduced as the density increases. Some spectral lines corresponding to transitions between the orbitals with higher principal quantum number disappear from the spectrum. Because of the pressure ionization effects, these orbitals move to the continuum.
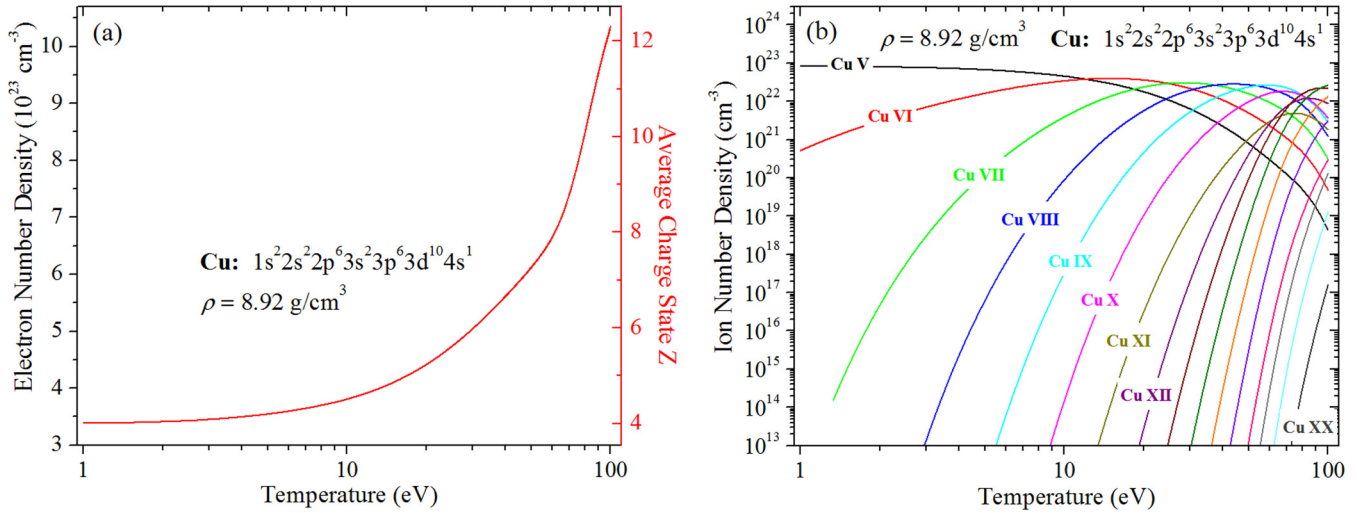
FIG. 5. (Color online) Electron number density and average charge state (a) and number density of ion species (b) in a solid-density copper plasma as a function of temperature.

The short-wavelength radiation emitted from dense plasmas, mainly in the x-ray and UV regions, is an important tool for plasma diagnostics, since the emitted spectrum can provide information about the plasma temperature and density conditions. In Fig. 7 the emissivity of copper plasma is shown for four temperatures, 20, 50, 70, and 100 eV. In each panel, the emission spectra are plotted for plasma densities of $0.01\rho_0$, $0.1\rho_0$, and ρ_0, where $\rho_0 = 8.92$ g/cm^3 is the solid-state density of copper. The emissivities are displayed in the soft x-ray and UV regions. At the solid density ρ_0, the most abundant charge state corresponds to Cu VI, Cu VIII, Cu IX, and Cu XIV ions for the temperatures of 20, 50, 70, and 100 eV, respectively [Fig. 5(b)]. For 20 eV [Fig. 7(a)] there is line emission at a density of $0.01\rho_0$ in the range from 6 to 30 nm. The most intense line is located at $\sim$17 nm, representing the crowding of the spectral line series due to the $3s^23p^2-3s^23p3d$ and $3s^23p-3s^23d$ transitions. As the density is increased by an

order of magnitude to $0.1\rho_0$, the emissivity of copper plasma is also increased. Many emission lines disappear in the spectrum due to the depression of the ionization potential, although the spectral line at $\sim$17 nm survives. At solid density ρ_0, there is no line emission present in the spectrum. The emissivity is higher, but the emitted radiation is continuous. As the temperature increases to 50 eV [Fig. 7(b)], more spectral lines are present in the soft x-ray region from 3 to 10 nm at a density of $0.01\rho_0$. The increase in density to $0.1\rho_0$ results in broadening, overlapping, and vanishing of these spectral lines. The emission line at $\sim$17 nm is still visible as a sharp peak. The plasma at solid-state density ρ_0 emits only continuous radiation. As the temperature increases further [Figs. 7(c) and 7(d)], the emission in lines intensifies in the spectral region between 2 and 10 nm at a density of $0.01\rho_0$. More line radiation with shorter wavelengths is emitted here. With the increase of density the spectral line emission in this region is significantly
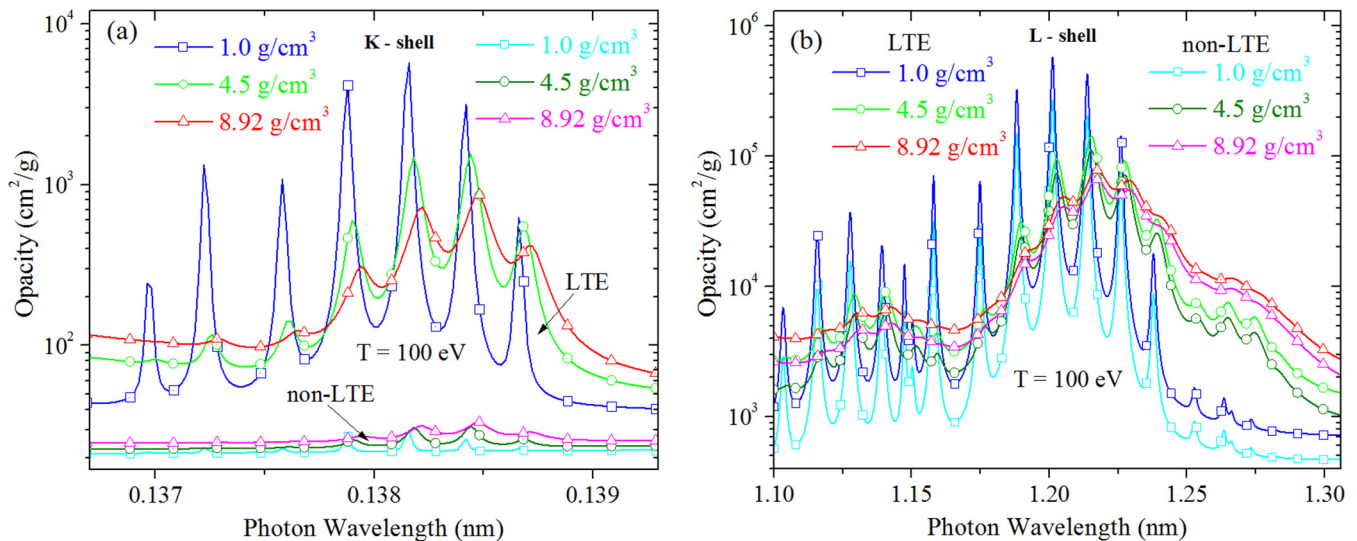

FIG. 6. (Color online) K-shell (a) and L-shell (b) spectral LTE and non-LTE opacities of copper plasma as a function of photon wavelengths at a temperature of 100 eV. The opacity spectra are shown for plasma densities of 1.0, 4.5, and 8.92 g/cm^3.
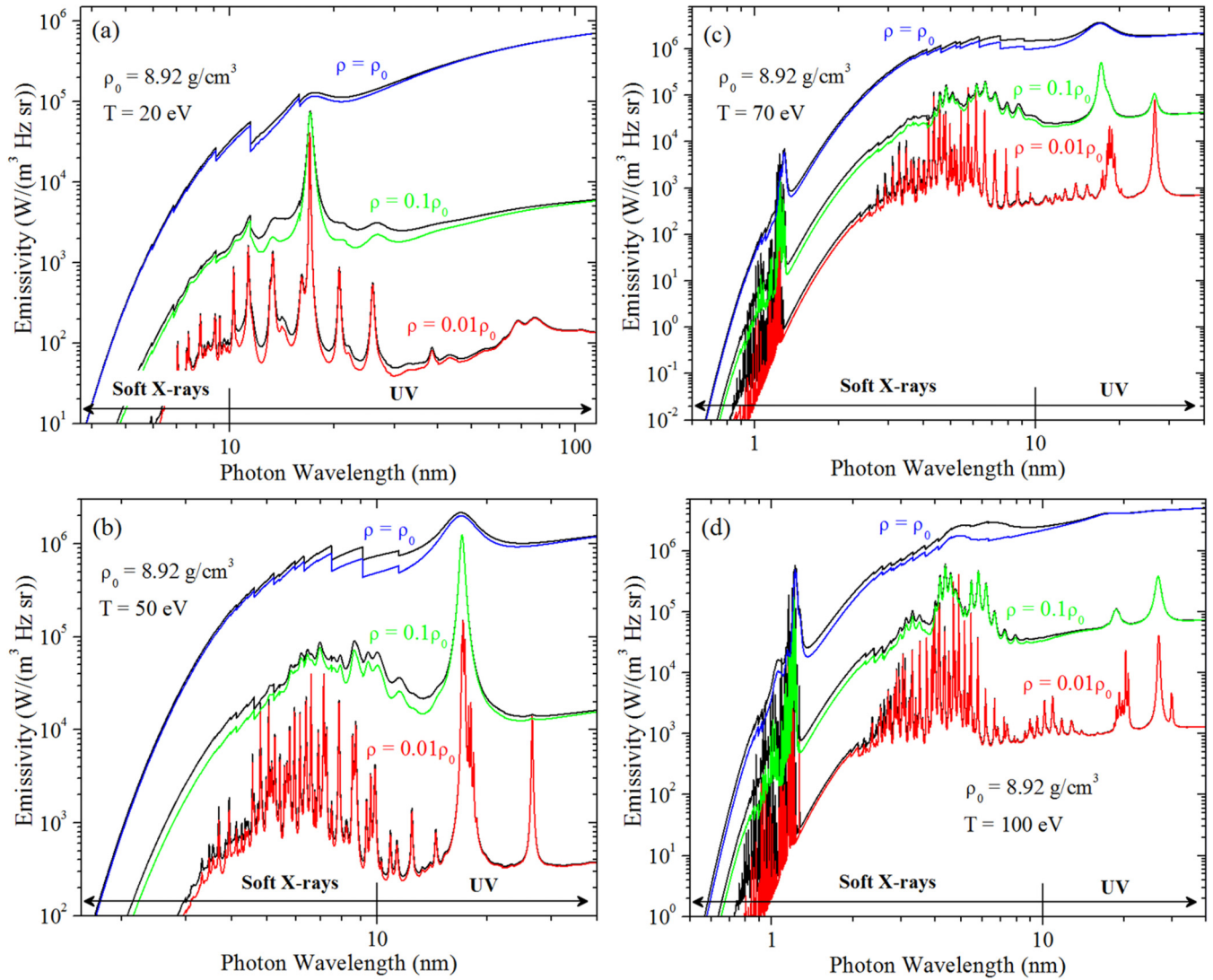
FIG. 7. (Color online) Spectrally resolved emissivities of copper plasma at temperatures of 20 eV (a), 50 eV (b), 70 eV (c), and 100 eV (d) as a function of photon wavelength. The regions of UV and soft x rays are marked by arrows. In each panel the emissivities are shown for mass densities of 0.0892, 0.892, and 8.92 g/cm^3. The LTE (black lines for all densities) and non-LTE (red, green, and blue lines corresponding to different densities) emissivities are compared.

suppressed. Soft x-ray emission from the L-shell and K-shell lines is also generated around 1 nm. The emission in this region of the spectrum has a very complex line structure. The radiation intensity of the spectral lines increases with both increasing density and temperature. It is seen that the non-LTE spectra differ from the LTE ones in this short-wavelength region. The agreement between the LTE and non-LTE emissivities is quite good for longer wavelengths. The deviations from the LTE predictions are larger for lower plasma densities and higher temperatures.

IV. CONCLUSIONS

Modeling of the optical properties of dense plasmas in the WDM regime is a challenging problem. There is a limited number of computational models that can reproduce properties of such plasmas in a self-consistent way. The *ab initio* HFS-CRSS model based on collisional-radiative kinetics was developed and applied to investigate the atomic and optical

properties of dense plasmas. The effects of a dense plasma environment on atomic levels of ions, such as continuum lowering, pressure ionization, energy level and line shifts, and spectral line broadening are implemented in this model. The REODP results on the average charge state, energy level shifts, opacities, and emissivities of dense plasmas were validated against the data available in the literature and showed a good agreement. The average charge state and number density of free electrons as a function of temperature were investigated for the solid-state density of copper plasma. It was found that four electrons from the outer $3d$ and $4s$ shells of copper atoms are ionized at temperature $\sim$1 eV. Under these plasma conditions the predominant charge state corresponds to the Cu V ions. The number density of ion species as a function of temperature in the range from 1 to 100 eV is also reported for the solid-state density of copper plasma.

It is commonly assumed that the LTE model is valid for the description of high-density plasmas. In LTE the electrons

and ions colliding at a high rate are in equilibrium, whereas photons are not in equilibrium with these plasma particles. Our HFS-CRSS study shows the importance of the non-LTE effects in the spectral region of soft x rays emitted from dense copper plasmas. A comparison between the LTE and non-LTE spectra of the K-shell and L-shell lines demonstrates that the non-LTE approach is necessary. The emissivity in the K-shell lines is completely suppressed and it is found to be lower in the L-shell lines, indicating that the energy-dissipating radiative processes are important in this soft x-ray region of the spectrum. It is observed that the radiation energy emitted in the soft x-ray and UV spectral regions provides very useful information about the thermodynamic state of the plasma (LTE or non-LTE) and the structure of emission lines and the continuous spectrum. We hope that the results of this work will be useful for future experimental studies of dense plasma effects on the opacity and emissivity of copper plasmas.

[1] J. D. Lindl, P. Amendt, R. L. Berger, S. G. Glendinning, S. H. Glenzer, S. W. Haan, R. L. Kauffman, O. L. Landen, and L. J. Suter, Phys. Plasmas **11**, 339 (2004).

[2] G. Mondet, F. Gilleron, J. C. Pain, A. Calisti, and D. Benredjem, High Energy Density Phys. **9**, 553 (2013).

[3] Z. R. Huang and K. J. Kim, Phys. Rev. Spec. Top.—Accel Beams **10**, 034801 (2007).

[4] P. R. Ribic and G. Margaritondo, J. Phys. D: Appl. Phys. **45**, 213001 (2012).

[5] F. J. Rogers and C. A. Iglesias, Science **263**, 50 (1994).

[6] A. N. Souza, D. J. Perkins, C. E. Starrett, D. Saumon, and S. B. Hansen, Phys. Rev. E **89**, 023108 (2014).

[7] W. L. Quan, Q. F. Chen, Z. J. Fu, X. W. Sun, J. Zheng, and Y. J. Gu, Phys. Rev. E **91**, 023106 (2015).

[8] S. X. Hu, L. A. Collins, V. N. Goncharov, T. R. Boehly, R. Epstein, R. L. McCrory, and S. Skupsky, Phys. Rev. E **90**, 033111 (2014).

[9] J. Osterholz, F. Brandl, M. Cerchez, T. Fischer, D. Hemmers, B. Hidding, A. Pipahl, G. Pretzler, S. J. Rose, and O. Willi, Phys. Plasmas **15**, 103301 (2008).

[10] R. W. Lee, S. J. Moon, H. K. Chung, W. Rozmus, H. A. Baldis, G. Gregori, R. C. Cauble, O. L. Landen, J. S. Wark, A. Ng *et al.*, J. Opt. Soc. Am. B **20**, 770 (2003).

[11] E. Stambulchik, V. Bernshtam, L. Weingarten, E. Kroupp, D. Fisher, Y. Maron, U. Zastrau, I. Uschmann, F. Zamponi, E. Forster *et al.*, J. Phys. A: Math. Theor. **42**, 214056 (2009).

[12] M. Koenig, A. Benuzzi-Mounaix, A. Ravasio, T. Vinci, N. Ozaki, S. Lepape, D. Batani, G. Huser, T. Hall, D. Hicks *et al.*, Plasma Phys. Controlled Fusion **47**, B441 (2005).

[13] P. A. Ni, M. I. Kulish, V. Mintsev, D. N. Nikolaev, V. Y. Ternovoi, D. H. H. Hoffmann, S. Udrea, A. Hug, N. A. Tahir, and D. Varentsov, Laser Part. Beams **26**, 583 (2008).

[14] G. Miloshevsky and A. Hassanein, IEEE Trans. Plasma Sci. **42**, 2508 (2014).

[15] D. Salzmann, *Atomic Physics in Hot Plasmas* (Oxford University Press, New York, 1998).

[16] G. Chiu and A. Ng, Phys. Rev. E **59**, 1024 (1999).

[17] J. M. Gil, R. Rodriguez, P. Martel, R. Florido, J. G. Rubiano, M. A. Mendoza, and E. Minguez, J. Quantum Spectrosc. Radiat. Transfer **114**, 136 (2013).

[18] C. Gao, J. L. Zeng, and J. M. Yuan, High Energy Density Phys. **7**, 54 (2011).

[19] J. Colgan, D. P. Kilcrease, N. H. Magee, G. S. J. Armstrong, J. Abdallah, M. E. Sherrill, C. J. Fontes, H. L. Zhang, and P. Hakel, High Energy Density Phys. **9**, 369 (2013).

[20] M. R. Zaghloul, Phys. Rev. E **69**, 026702 (2004).

[21] H. K. Chung, C. Bowen, C. J. Fontes, S. B. Hansen, and Y. Ralchenko, High Energy Density Phys. **9**, 645 (2013).

[22] J. Clerouin, G. Robert, P. Arnault, C. Ticknor, J. D. Kress, and L. A. Collins, Phys. Rev. E **91**, 011101(R) (2015).

[23] A. BarShalom, J. Oreg, and M. Klapisch, Phys. Rev. E **56**, R70 (1997).

[24] M. Klapisch, A. Bar-Shalom, J. Oreg, and D. Colombant, Phys. Plasmas **8**, 1817 (2001).

[25] R. Florido, R. Rodriguez, J. M. Gil, J. G. Rubiano, P. Martel, E. Minguez, and R. C. Mancini, Phys. Rev. E **80**, 056402 (2009).

[26] C. Gao, J. L. Zeng, Y. Q. Li, F. T. Jin, and J. M. Yuan, High Energy Density Phys. **9**, 583 (2013).

[27] F. E. Irons, J. Quantum Spectrosc. Radiat. Transfer **22**, 1 (1979).

[28] G. V. Miloshevsky, V. I. Tolkach, S. Rozin, and G. Shani, Nucl. Instrum. Methods Phys. Res. B **168**, 467 (2000).

[29] S. S. Harilal, G. V. Miloshevsky, T. Sizyuk, and A. Hassanein, Phys. Plasmas **20**, 013105 (2013).

[30] V. Tolkach, V. Morozov, and A. Hassanein, Argonne National Laboratory Report No. ANL-ET/02-23, 2002 (unpublished).

[31] J. C. Slater, Phys. Rev. **81**, 385 (1951).

[32] C. Moller and M. S. Plesset, Phys. Rev. **46**, 618 (1934).

[33] C. F. Fischer, Comput. Phys. Rep. **3**, 274 (1986).

[34] C. D. Sherrill and H. F. Schaefer, Adv. Quantum Chem. **34**, 143 (1999).

[35] S. Ichimaru, Rev. Mod. Phys. **54**, 1017 (1982).

[36] J. C. Stewart and K. D. Pyatt, Astrophys. J. **144**, 1203 (1966).

[37] R. M. More, Lawrence Livermore National Laboratory Report No. UCRL-84991, 1981 (unpublished).

[38] S.-K. Son, R. Thiele, Z. Jurek, B. Ziaja, and R. Santra, Phys. Rev. X **4**, 031004 (2014).

[39] Y. Q. Li, J. H. Wu, Y. Hou, and J. M. Yuan, J. Phys. B: At. Mol. Opt. Phys. **42**, 235701 (2009).

[40] S. Mazevet, M. P. Desjarlais, L. A. Collins, J. D. Kress, and N. H. Magee, Phys. Rev. E **71**, 016409 (2005).

[41] F. Perrot and M. W. C. Dharmawardana, Phys. Rev. E **52**, 5352 (1995).

[42] S. P. Lyon and J. D. Johnson, Los Alamos National Laboratory Report No. LA-UR-92-3407, 1992 (unpublished).

[43] R. M. More, K. H. Warren, D. A. Young, and G. B. Zimmerman, Phys. Fluids **31**, 3059 (1988).

[44] R. P. Feynman, N. Metropolis, and E. Teller, Phys. Rev. **75**, 1561 (1949).

[45] T. R. Preston, S. M. Vinko, O. Ciricosta, H. K. Chung, R. W. Lee, and J. S. Wark, High Energy Density Phys. **9**, 258 (2013).